INTERNATIONAL JOURNAL FOR NUMERICAL METHODS IN FLUIDS
Int. J. Numer. Meth. Fluids 2005; **47**:233–251
Published online 9 November 2004 in Wiley InterScience (www.interscience.wiley.com). DOI: 10.1002/fld.806

Internal wave computations using the ghost fluid method on unstructured grids

Sangmook Shin*,†

Naval Systems Development Center, Agency for Defense Development, Jinhae, South Korea

SUMMARY

Two-layer incompressible flows are analysed using the ghost fluid method on unstructured grids. Discontinuities in dynamic pressure along interfaces are captured in one cell without oscillations. Because of data reconstructions based on gradients, the ghost fluid method can be adopted without additional storages for the ghost nodes at the expense of modification in gradient calculations due to the discontinuity.

The code is validated through comparisons with experimental and other numerical results. Good agreements are achieved for internal waves generated by a body moving at transcritical speeds including a case where upstream solitary internal waves propagate. The developed code is applied to analyse internal waves generated by a NACA0012 section moving near interfaces. Variations of the lift acting on the body and configurations of the interfaces are compared for various distances between the wing and the interface. The effects of the interface are compared with the effects of a solid wall. Copyright © 2004 John Wiley & Sons, Ltd.

KEY WORDS: discontinuity; interface; two-layer incompressible fluids; solitary internal wave; unstructured grid

1. INTRODUCTION

Flows of two incompressible fluids encompass a wide range of engineering problems such as bubble dynamics and oil extraction from an underground reservoir. In the ocean, a density gradient due to a vertical temperature variation is frequently confined within a thin pycnocline which separates two well-mixed fluid layers. Since the pycnocline is thin compared with characteristic length of the flow, the internal waves also can be modelled using two-layer incompressible flows. Internal waves are related to several important problems such as variations of the force acting on the body moving near an interface and effects on a sonar performance.

There are many studies for computing flow of two incompressible fluids separated by a moving surface of discontinuity [1–5]. Most of the previous studies are based on δ-function

*Correspondence to: S. Shin, Naval Systems Development Center, Agency for Defense Development, P.O. Box 18, Jinhae, 645-600, South Korea.
†E-mail: smshin@add.re.kr

Received 19 May 2004
Revised 16 September 2004

formulations. For those methods, the variations of the material properties are smoothed over a few grid cells to avoid difficulties caused by the discontinuity. Although the smoothing can provide robustness of the scheme with ease, it introduces numerical smearing across the interface. The smearing causes compressibility near the interface so that the continuity equation cannot be satisfied for each material [6]. The inaccuracy caused by the smoothing may depend on the smoothing width relative to the flow scale and the order of the scheme in space may be degraded. To avoid the inaccuracy due to the smoothing, Helenbrook *et al.* suggests a method to treat the discontinuity in the interface of the incompressible fluids [5]. The method treats the surface of the discontinuity as a moving boundary which subdivides the domain into two regions. Although the scheme maintains a second-order accuracy in space, the scheme has difficulty handling high curvature or merging interfaces.

To handle the discontinuity in entropy along the interface of two compressible fluids, the ghost fluid method is suggested by Fedkiw *et al.* [7]. The method treats the discontinuity as a moving boundary also, but it provides more flexibility to treat various jump conditions. The ghost fluid method can capture the discontinuity without smearing or oscillation based on discretizations of two continuous fields for both fluids along the interface. Recently the ghost fluid method is successfully applied to various problems. The strong shock impact on the interface of compressible materials is investigated using the ghost fluid method by Liu *et al.* [8]. The ghost fluid method is also used to create accurate discretizations across the interface of the compressible and incompressible regions [9] and the interface of the two-phase incompressible flow including effects of viscous and surface tension [10]. Fedkiw expands the ghost fluid method to couple an Eulerian fluid model to a Lagrangian solid model [11].

In this study, the ghost fluid method is adopted to analyse flow fields containing sharp discontinuities along interfaces of two incompressible fluids using unstructured grids. The MUSCL type method is used and higher-order accuracy in space is achieved based on the gradients of dependent variables which are stored at nodes so that the flux calculation does not require explicit use of a wider stencil. Because of that feature of unstructured grid method, the ghost fluid method can be adopted efficiently so that dependent variables of ghost fluids are constructed only for control surfaces which are assigned to edges crossing the interface. The modification required for the gradient calculations near the interface can be handled also efficiently by the same method which is used for the flux calculation. The ghost fluid method is coupled with a time accurate incompressible solver which is based on dual time stepping with an implicit method although the ghost fluid method is usually coupled with an explicit time marching scheme previously.

A time accurate incompressible solver on an unstructured grid which uses a level set method to track particles [12, 13] is expanded to adopt the ghost fluid method. To validate the developed code, transcritical internal waves are computed and the results are compared with experimental and other computational results. The code is applied to analyse internal waves generated by a NACA0012 section moving near the interface and the effects of the interface on the lift acting on the body is compared with the effects of a solid wall.

2. NUMERICAL METHODS

2.1. Governing equations and a node-based finite volume method

The governing equations for both materials are unsteady incompressible Euler equations. The focus of this study is to handle a discontinuity in the density across an interface of two

incompressible fluids. Since both materials are incompressible, the densities can be eliminated from the governing equations except the pressure terms which are divided by densities. The non-dimensionalization based on the density of each material and the same reference velocity makes the two governing equation sets identical. All effects of the discontinuity in the density are confined to discontinuity in the non-dimensionalized pressure. The dynamic pressure is used as a dependent variable which is the perturbation to hydrostatic pressure. The effects of the gravity are considered separately to enforce continuity of pressure along interfaces as explained latter. To track fluid particles, the level set function ϕ is coupled with the governing equations. For an arbitrary control volume Ω, whose control surface is $\partial\Omega$, the governing equations can be written as follows for both materials:

$$\frac{\partial}{\partial t}\int_{\Omega} Q\,\mathrm{d}V + \oint_{\partial\Omega} F_{\mathrm{inv}}\,\mathrm{d}S = 0 \tag{1}$$

For a two-dimensional case,

$$Q = \begin{bmatrix} 0 \\ u \\ v \\ \phi \end{bmatrix}, \quad F_{\mathrm{inv}} = \begin{bmatrix} \Theta \\ u\Theta + pn_x \\ v\Theta + pn_y \\ \phi\Theta \end{bmatrix}, \quad \Theta = un_x + vn_y \tag{2}$$

A node-based finite volume method is used to discretize the governing equations spatially where all the dependent variables are defined at the vertices of the grid. A non-overlapping control volume surrounding each node is defined by control surface portions connecting the centroid of the element to the midpoint of boundary of the element.

2.2. Dual time stepping using an implicit method with respect to pseudotime

Time derivatives in the governing equations are replaced with a second-order backward difference formula.

$$\left.\frac{\partial u}{\partial t}\right|^n \approx \frac{3u^n - 4u^{n-1} + u^{n-2}}{2\Delta t} \tag{3}$$

For each physical time step, artificial compressibility with respect to pseudotime τ is introduced.

$$V_i \frac{\partial}{\partial \tau}\begin{bmatrix} \tilde{p}_i \\ \tilde{u}_i \\ \tilde{v}_i \\ \tilde{\phi}_i \end{bmatrix} + \frac{1.5V_i}{\Delta t}\begin{bmatrix} 0 \\ \tilde{u}_i \\ \tilde{v}_i \\ \tilde{\phi}_i \end{bmatrix} + \tilde{R}_i(\tilde{p},\tilde{u},\tilde{v},\tilde{\phi}) = \frac{V_i}{\Delta t}\begin{bmatrix} 0 \\ 2u^{n-1} - 0.5u^{n-2} \\ 2v^{n-1} - 0.5v^{n-2} \\ 2\phi^{n-1} - 0.5\phi^{n-2} \end{bmatrix} \tag{4}$$

where V_i is the size of the control volume of the ith node and $\tilde{R}_i(\tilde{p},\tilde{u},\tilde{v},\tilde{\phi})$ is the residual at the ith node based on the intermediate dependent variables set $(\tilde{p},\tilde{u},\tilde{v},\tilde{\phi})$ with the modification

in the continuity equation due to the artificial compressibility,

$$\tilde{F}_{\text{inv}} = \begin{bmatrix} \beta\tilde{\Theta} \\ \tilde{u}\tilde{\Theta} + \tilde{p}n_x \\ \tilde{v}\tilde{\Theta} + \tilde{p}n_y \\ \tilde{\phi}\tilde{\Theta} \end{bmatrix}, \quad \tilde{\Theta} = \tilde{u}n_x + \tilde{v}n_y \tag{5}$$

where β is the artificial compressibility parameter. Once the steady solution with respect to the pseudotime τ is obtained, it is substituted for the dependent variables set at new time step (p^n, u^n, v^n, ϕ^n). To get the steady solution with respect to the pseudotime τ, an implicit method is used which is based on a linearized Euler backward method with a local time stepping. The scheme is stable for any combination of the physical time step size Δt and the pseudotime step size $\Delta\tau$. The physical time step size Δt can be increased arbitrarily provided that the time step size is small enough to resolve variations of the flow field in time using the second-order backward difference formula (3). The pseudotime step size $\Delta\tau$ is decided to accelerate the convergence to the steady state with respect to the pseudotime τ. Although the scheme is stable at very large local Courant number, there is an optimal pseudotime step size $\Delta\tau$ because the large Courant number reduces the diagonal dominance of the implicit matrix. A typical value of the local Courant number used in this study is 200.

2.3. Numerical fluxes through a control surface portion assigned to an edge

Contributions of the inviscid fluxes to the residual of each node are considered based on the numerical flux through a control surface portion which is assigned to an edge. The dependent variable sets Q_L and Q_R at both sides of the control surface portion are reconstructed using gradients of the dependent variables which are stored at nodes.

$$Q_L = Q_{\text{node 1}} + \nabla Q|_{\text{node 1}} \cdot (\mathbf{r}_{\text{c.s.}} - \mathbf{r}_{\text{node 1}}), \quad Q_R = Q_{\text{node 2}} + \nabla Q|_{\text{node 2}} \cdot (\mathbf{r}_{\text{c.s.}} - \mathbf{r}_{\text{node 2}}) \tag{6}$$

The gradients of the dependent variables are calculated using Green–Gauss theorem.

$$\nabla Q \approx \frac{1}{\text{Volume}} \oint_{\partial\Omega} Q\mathbf{n}\,\mathrm{d}S \tag{7}$$

The above integration is carried out along each control surface portion which is assigned to an edge.

Roe's flux difference splitting method is used to calculate the inviscid fluxes for the governing equations which are coupled with the transport equation of the level set function ϕ.

$$F_{\text{inv}} = \frac{1}{2}[F(Q_L) + F(Q_R)] - \frac{1}{2}|\hat{A}|(Q_R - Q_L) \tag{8}$$

For the flux Jacobian, there is a repeated eigenvalue. However, there are linearly independent eigenvectors corresponding to the repeated eigenvalue so that the flux Jacobian is diagonalizable with real eigenvalues. Similarly to the case of the artificial compressibility method without the level set function ϕ, it can be easily shown that the jump condition is satisfied with the

flux Jacobian matrix based on the simple algebraic average of the dependent variables.

$$\begin{aligned} \hat{A}(Q_R - Q_L) &= F(Q_R) - F(Q_L) \\ \hat{A}(Q_L, Q_R) &= \left.\frac{\partial F}{\partial Q}\right|_{Q=\bar{Q}}, \quad \bar{Q} = \frac{1}{2}(Q_L + Q_R) \end{aligned} \tag{9}$$

2.4. Flux calculations for edges crossing an interface using the ghost fluid method

The main idea of the ghost fluid method [7] is that the two-fluid flow containing a contact discontinuity may be regarded as a combination of two single phase flow fields which satisfy certain conditions across an interface. The required conditions should guarantee that the resultant flow fields satisfy the physical conservation laws in the neighbourhood of the interface. The required conditions across an interface for the present problem can be set up as follows. In Figure 1, a control volume moving with an interface is shown. Since both materials are incompressible, the conservation of the mass requires the continuity of the normal velocity across an interface. In this study, surface tension is neglected so that the momentum conservation in normal direction requires the continuity of pressure across an interface.

$$V_{1n} = V_{2n} \tag{10}$$

$$P_1 = P_2 \tag{11}$$

The requirement of the continuity of pressure (11) introduces a discontinuity across an interface in dynamic pressures which are non-dimensionalized based on the densities of the materials. For the location where an interface elevation is η and pressure coefficients are C_{p1}, C_{p2} for two materials, respectively, the continuity of pressure requires the following

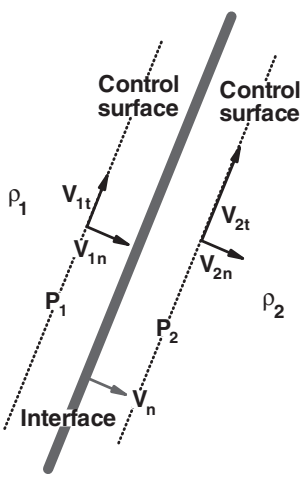

Figure 1. A control volume around a discontinuity across an interface.

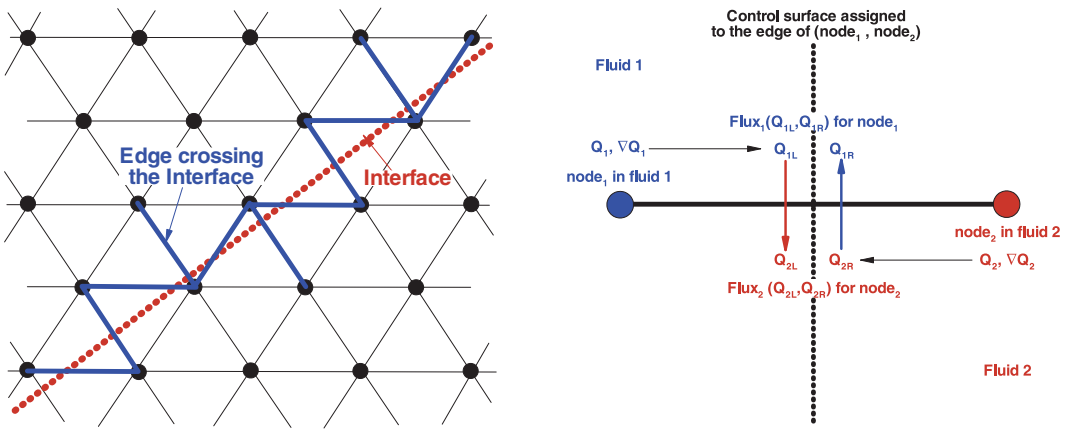

Figure 2. Edges crossing an interface and two fluxes across a control surface assigned to the edge.

relationships in the two pressure coefficients:

$$C_{p1} = C_{p2}\frac{\rho_2}{\rho_1} + 2\left(1 - \frac{\rho_2}{\rho_1}\right)\frac{g\eta}{V_\infty^2} \tag{12}$$

$$C_{p2} = C_{p1}\frac{\rho_1}{\rho_2} + 2\left(1 - \frac{\rho_1}{\rho_2}\right)\frac{g\eta}{V_\infty^2} \tag{13}$$

Based on relationships (10), (12) and (13), the dependent variables of the ghost fluids can be constructed. For the inviscid calculations, the tangential velocities of ghost fluids may be given based on a one-sided extrapolation.

In the original work of Fedkiw *et al.* [7], the dependent variable vectors at the ghost nodes are stored for all nodes although it is pointed out that the use of the ghost nodes may be restricted in the neighbourhood of the interface according to the stencils for flux calculations. In this study, the ghost fluid method is adopted without an additional storage for the ghost nodes since the higher-order accuracy is attained based on the gradients stored at nodes. However, the gradients near an interface should be calculated carefully due to the discontinuity along the interface. Since the integrations for the residual and gradient calculations are carried out along the control surface portions which are assigned to edges, the same method can be applied to treat the discontinuity for both gradient and flux calculations.

For the integration along the control surface portion assigned to an edge, it can be checked whether the edge crosses the interface or not, simply based on the signs of level set function at two nodes of the edge. If an edge crosses the interface, the integration should be modified to include the effects of the discontinuity using the ghost fluid method. The left figure of Figure 2 shows an interface and edges whose two nodes are included in different materials. For the gradient calculations, the dependent variables at the control surface are assumed as averages of the dependent variables at both nodes if the two nodes are included in the same material. However, if the edge crosses the interface, two different averages are calculated for both materials using dependent variables of ghost fluid and real fluid. The right figure

of Figure 2 shows the procedure to calculate two fluxes for the edge crossing the interface. Based on the dependent variables and gradients, dependent variable vectors of real fluid Q_{1L} and Q_{2R} are calculated for fluid 1 and 2. Then dependent variable vectors of ghost fluid Q_{2L} and Q_{1R} are constructed from Q_{1L} and Q_{2R} using (10), (12) and (13). From the Q_L and Q_R for each fluid, two fluxes are calculated using Roe's flux difference splitting method. The appropriate flux is added or subtracted for the residual of each control volume.

Whenever the level set function is updated, it is checked whether the sign of the level set function at a node is changed or not during the time step for each node. If the sign of the level set function is changed at a node then the dependent variables at the node are adjusted to consider the change of material. Since the time derivatives are replaced with the three-point backward difference formula (3), old dependent variables should be adjusted also. The implicit matrix also should be adjusted to include the effects of the ghost fluid method near the interface. Whenever Q_L or Q_R is modified due to the ghost fluid method, the effects of the modification on the implicit matrix are considered using a chain rule.

$$\frac{\partial F}{\partial Q_{\text{real}}} = \frac{\partial F}{\partial Q_{\text{ghost}}} \frac{\partial Q_{\text{ghost}}}{\partial Q_{\text{real}}} \tag{14}$$

3. RESULTS AND DISCUSSIONS

The time accurate incompressible flow solver is developed and validated through comparisons with experimental and computational results for the vortex shedding behind a circular cylinder [12]. To validate the particle tracking algorithm using the level set method, streaklines are constructed based on the contours of the level set function which is calculated without re-initialization steps. The results are compared with flow visualization results and good agreements are achieved [13]. In this study, the code is expanded for flows of two incompressible fluids using the ghost fluid method. To validate the developed code, internal waves are computed which are generated by a body moving at transcritical speeds near an interface of fresh water and kerosene. The results are compared with experimental and other computational results. Finally the code is applied to analyse the internal waves generated by a NACA0012 section moving near the interface. Grid dependency study is carried out using three different size grids and the effects of the time step size Δt are shown. The effects of the interface on the lift acting on the body are compared with the effects of a solid wall.

3.1. Code validation through comparisons of results of transcritical internal waves

Experiments are carried out for a two-layer flow over a topography by Melville and Helfrich [14]. In the study, the inhomogeneous extended Korteweg–de Varies (EKdV) equation is also analysed numerically. Grue *et al.* [15] investigated the same problem using the fully non-linear potential method. In Figure 3, a schematic drawing for the experiments is shown. The experiments are carried out using an upper layer of dyed kerosene ($\rho = 0.80\ \text{g/cm}^3$) and a lower layer of fresh water ($\rho = 0.986\,\text{g/cm}^3$). The displacements of the interface are measured by a camera which is fixed 5 m downstream of the starting location of the topography. For the selected cases, the depths of kerosene and water are 3 and 12 cm, respectively. The internal waves are generated by a moving body in the upper layer with a profile given by $H = \tilde{H}_0 \sec h^2(Kx)$, $\tilde{H}_0 = 5.1$ cm, $K = 0.039\ \text{cm}^{-1}$. The depth of the submerged body is 0.4

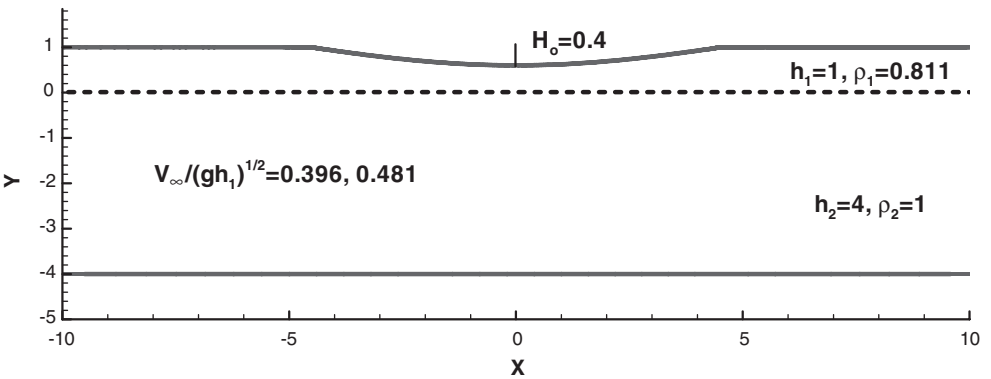

Figure 3. A schematic drawing of the two-layer flow experiments by Melville and Helfrich [14].

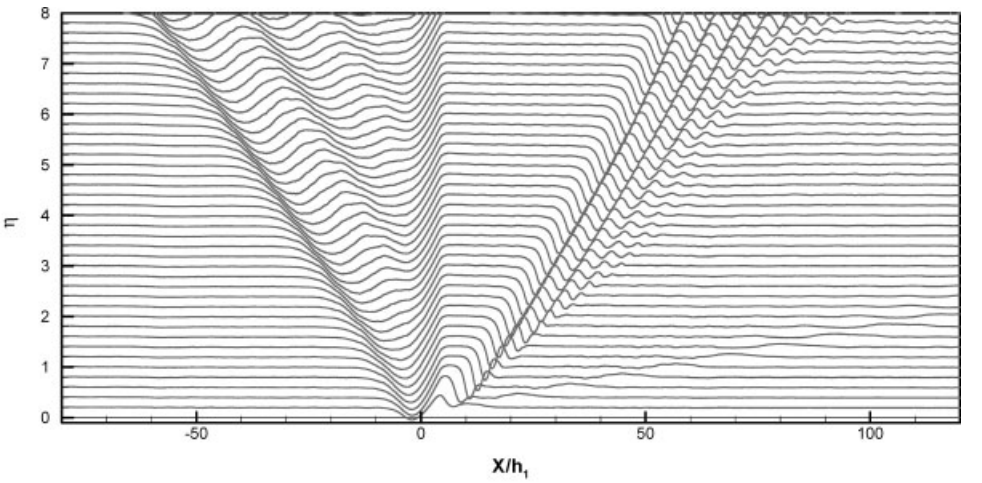

Figure 4. Time evolution of an interface: $V_\infty/\sqrt{gh_1} = 0.396$.

of the upper layer thickness, 1.2 cm. The body is towed at various speeds and two cases are computed for $V_\infty/\sqrt{gh_1} = 0.396$ and 0.481. Those speeds correspond to $0.94c_0, 1.14c_0$, respectively, where c_0 is the reference speed used by Grue *et al.* $c_0^2 = [gh_1h_2(\rho_2 - \rho_1)]/(\rho_1 h_2 + \rho_2 h_1)$. Although the top of the upper fluid is a free surface in the experiments, both of the EKdV and the fully non-linear potential calculations treat the upper boundary as a rigid lid. In this calculation, the upper boundary is also considered as an inviscid wall. Except inflow and out flow boundaries, all other boundaries are considered as inviscid walls including the body surface. Physical time step size Δt is set to be 0.1.

In Figure 4, the time evolution of the interface is shown for $V_\infty/\sqrt{gh_1} = 0.396$. For this speed, solitary internal waves are generated periodically and propagate upstream. In the behind of the body an elevated plateau of the interface expands continuously and waves move downstream behind the plateau. Since the interface configuration varies continuously, the in-

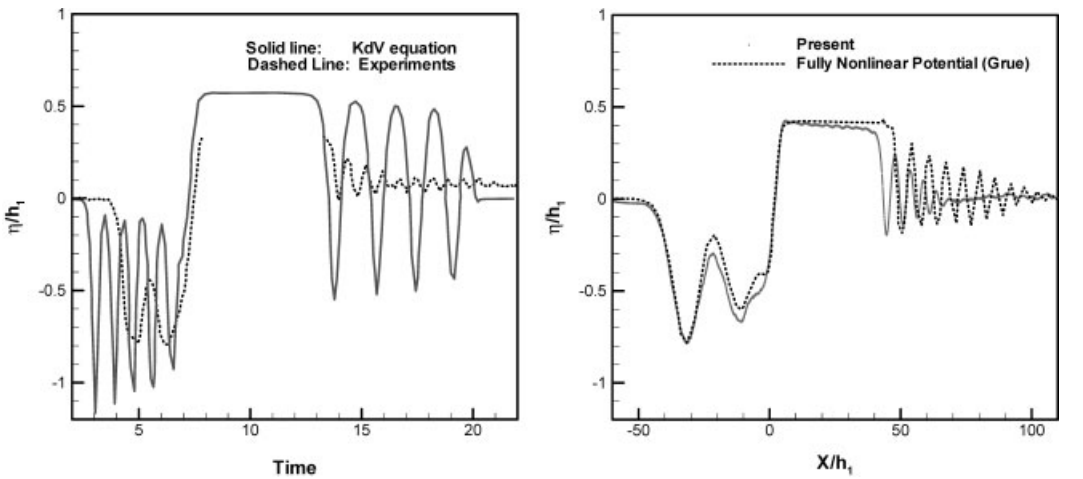

Figure 5. Comparisons of an interface elevation: $V_\infty/\sqrt{gh_1} = 0.396, V_\infty t/h_1 = 170$.

terface elevation at a moment and the measured time history of the interface at one point may not be compared directly. However, the comparison is made based on the interface elevation at the time when the body approximately passes the camera in Grue *et al*. In this study a comparison is made at the moment $V_\infty t/h_1 = 170$. During the time duration, the body moves 5.1 m. In Figure 5, the measurements and three numerical results are shown. For the results of the EKdV equation, both of upstream solitary waves and downstream waves show large discrepancy. The elevation of the plateau is also overestimated. However, the present calculations and the results of the fully non-linear potential achieve good agreements.

For the downstream waves, contours of non-dimensionalized pressure are shown in Figure 6. Contrary to non-linear free surface waves, it can be seen that the wave has flatter configuration in crest. This tendency can be seen more clearly in the results of EKdV of Figure 5. The thickness of the upper layer is considered as a reason for the flatter crest. Since the thickness of the upper layer is thinner than that of the lower layer, an increase in mean velocity of the upper layer is more significant when the depth is changed due to the elevation of the interface. Because of the increased velocity, higher gradients in dynamic pressure field will be produced if the radii of curvature of particle paths are same. However, the dynamic pressure gradients should be appropriate to maintain the continuity of pressure across the interface. To compensate the increase in dynamic pressure gradients due to the acceleration of the mean velocity, the radius of curvature should be increased for regions where the accelerations appear.

The time evolution of the interface for $V_\infty/\sqrt{gh_1} = 0.481$ is shown in Figure 7. The ratio of the towed speed to the reference speed defined in Grue *et al*. is 1.14. In this case the upstream solitary waves are not generated and the elevation of the plateau is decreased. The measured interface and numerical results are compared in Figure 8. Although the present results predict slightly larger depression of the interface, both of the present results and the fully non-linear potential results underestimate the depression of the interface in front of the body. In the experiments, no significant surface waves are reported. However, it is

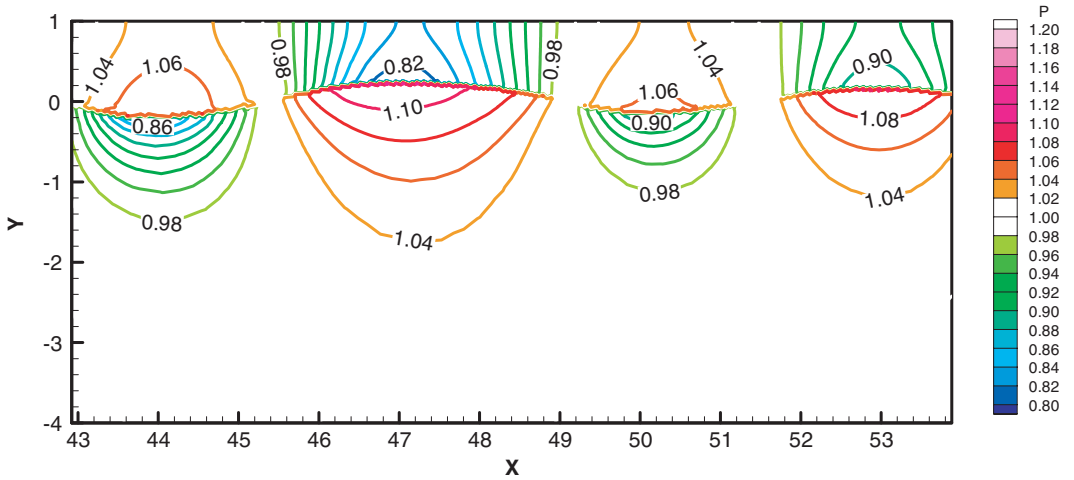

Figure 6. A downstream wave profile: $V_\infty/\sqrt{gh_1} = 0.396, V_\infty t/h_1 = 170$.

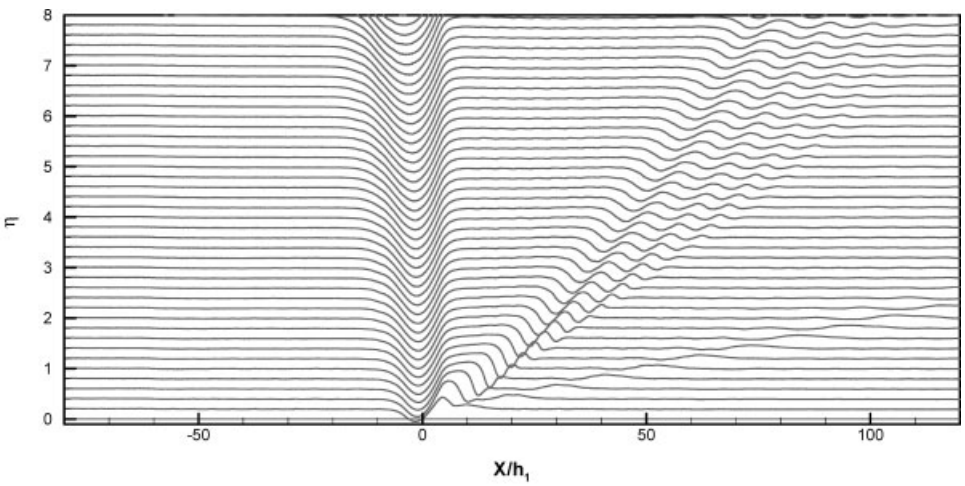

Figure 7. Time evolution of an interface: $V_\infty/\sqrt{gh_1} = 0.481$.

not clear that the assumption of the rigid wall for the upper boundary do not have effects on the interface elevations. As mentioned in the following section, the interface has significant effects on the flow field even though the elevations of the interface are not obvious.

3.2. Internal waves generated by a NACA0012 section moving near an interface

The developed code is applied to analyse internal waves generated by a NACA0012 section which moves near an interface. The density ratio of two materials ρ_1/ρ_2 is 0.811 and Froude

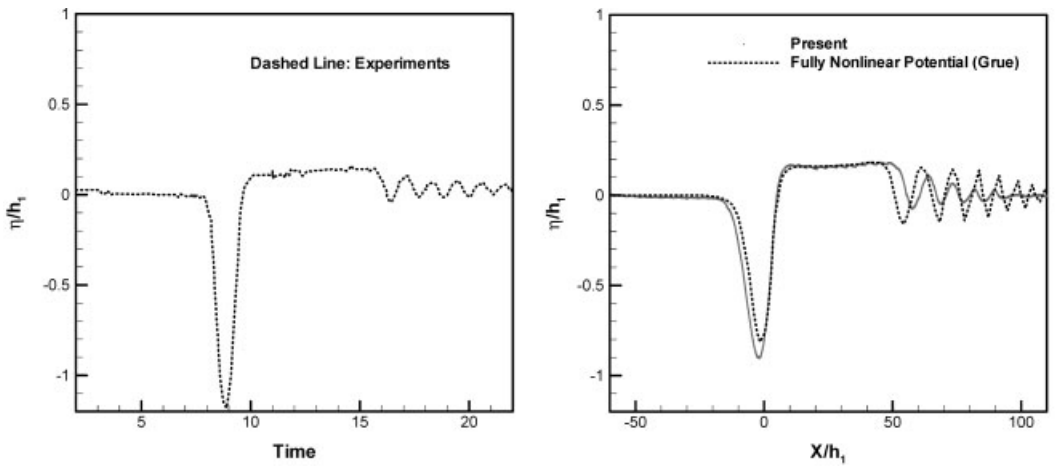

Figure 8. Comparisons of an interface elevation: $V_\infty/\sqrt{gh_1} = 0.481, V_\infty t/h_1 = 170$.

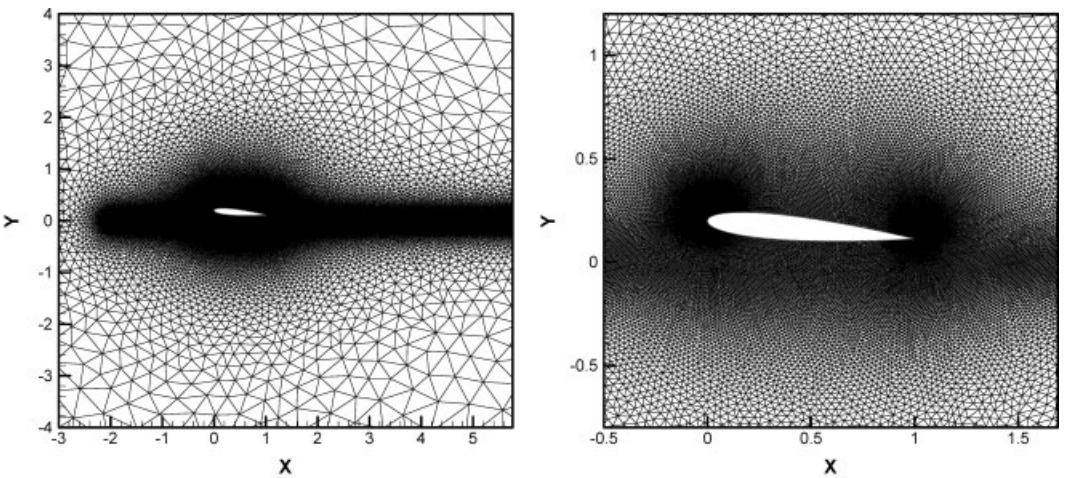

Figure 9. An unstructured grid around a NACA0012 section near an interface.

number based on the chord of the wing section $V_\infty/\sqrt{gc}$ is 0.3. The angle of attack of the wing section is 5°. The distance between the wing section and the undisturbed interface is varied. The undisturbed interface is located at $Y = 0$ always and the location of the wing is indicated by the Y-co-ordinate of the leading edge Y_n. On the upper and lower boundaries of the computational domain, far field boundary conditions are applied. Physical time step size Δt is set to be 0.1 except in Figure 14, where the time step size is varied to investigate the dependency of the results on the time step size. In Figure 9, an unstructured grid around the NACA0012 section near the interface is shown for the case of $Y_n = 0.2$. Due to the flexibility of the unstructured grid, grid clustering can be achieved easily regardless of the

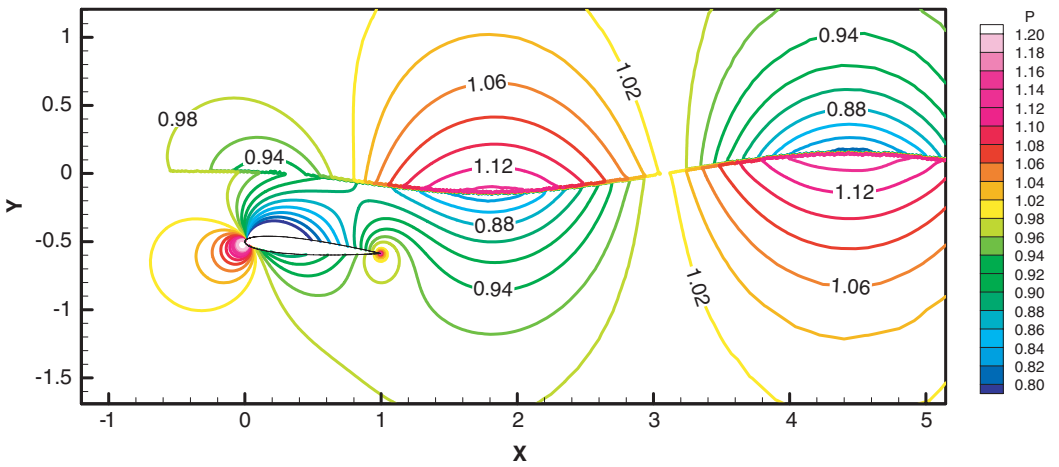

Figure 10. Non-dimensionalized pressure contours around a NACA0012 section near an interface: $Y_n = -0.5, V_\infty/\sqrt{gc} = 0.3$.

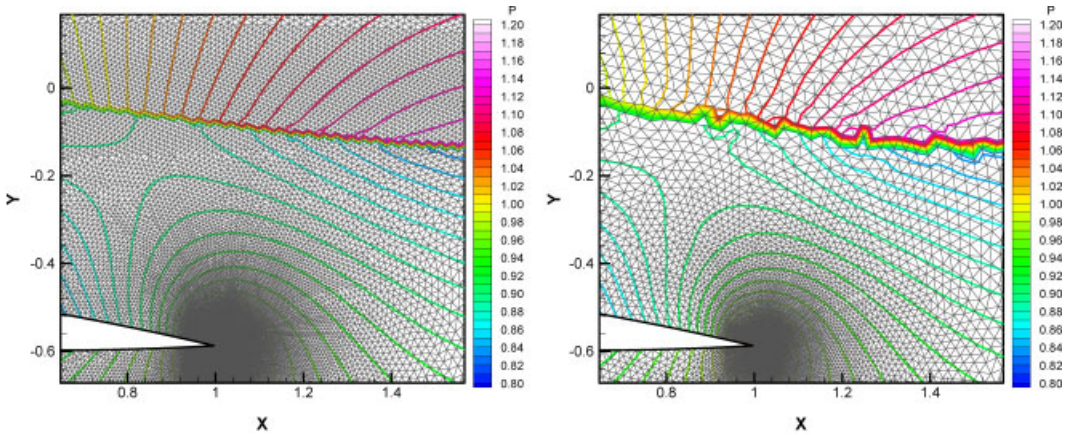

Figure 11. Non-dimensionalized pressure contours and grids near a trailing edge: $Y_n = -0.5$, $V_\infty/\sqrt{gc} = 0.3$.

distance between the wing section and the interface. Since Euler equations are analysed, a viscous grid around the body and wake is not used.

Figure 10 shows non-dimensionalized pressure contours along the interface for the case of $Y_n = -0.5$. In the lower layer, the dynamic pressure increases at crest and decreases at trough. However, the variations in the dynamic pressure are reversed in the upper layer and dynamic pressures have opposite signs for two layers. For this case, the density of the upper layer is comparable to the density of the lower layer so that the differences in hydrostatic pressure across the interface are small compared to magnitude of the hydrostatic pressure corresponding to the elevation of the interface. To satisfy the continuity of pressure, the

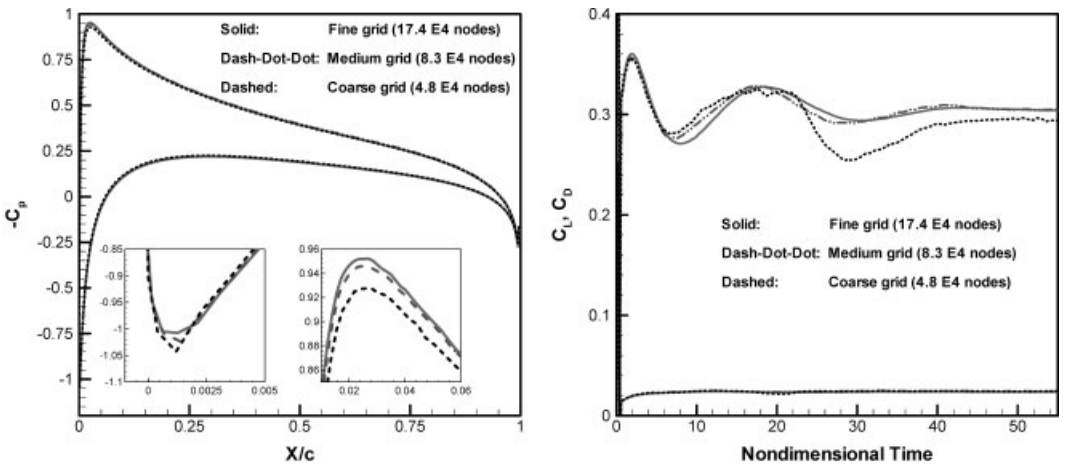

Figure 12. Grid dependency of pressure coefficient distributions on a NACA0012 section near an interface: $Y_n = -0.5$, $V_\infty/\sqrt{gc} = 0.3$.

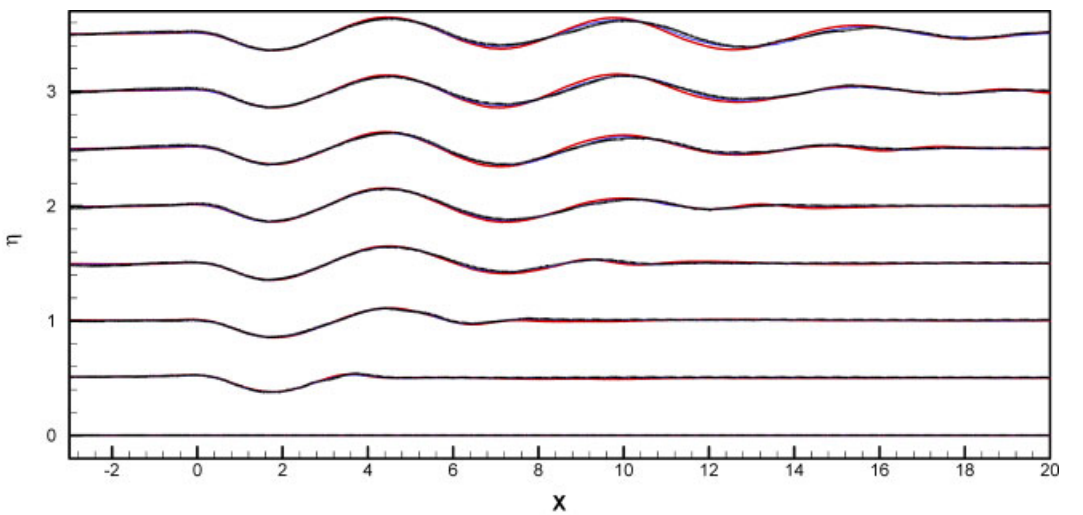

Figure 13. Grid dependency of calculated wave profiles: $Y_n = -0.5, V_\infty/\sqrt{gc} = 0.3$.

differences in dynamic pressure across the interface should be also small. Because dynamic pressures have opposite signs for two layers, the magnitude of the dynamic pressure should be small compared to the hydrostatic pressure. It implies that the pressures on the interface are dominated by the hydrostatic pressure due to the elevation of the interface and the dynamic pressure cannot compensate the whole variations in hydrostatic pressure along the interface. If the density of the upper layer is negligible compared to the density of the lower layer, the dynamic pressure should compensate the most of the variations in hydrostatic pressure along the interface because the variations in the hydrostatic and dynamic pressure in the upper

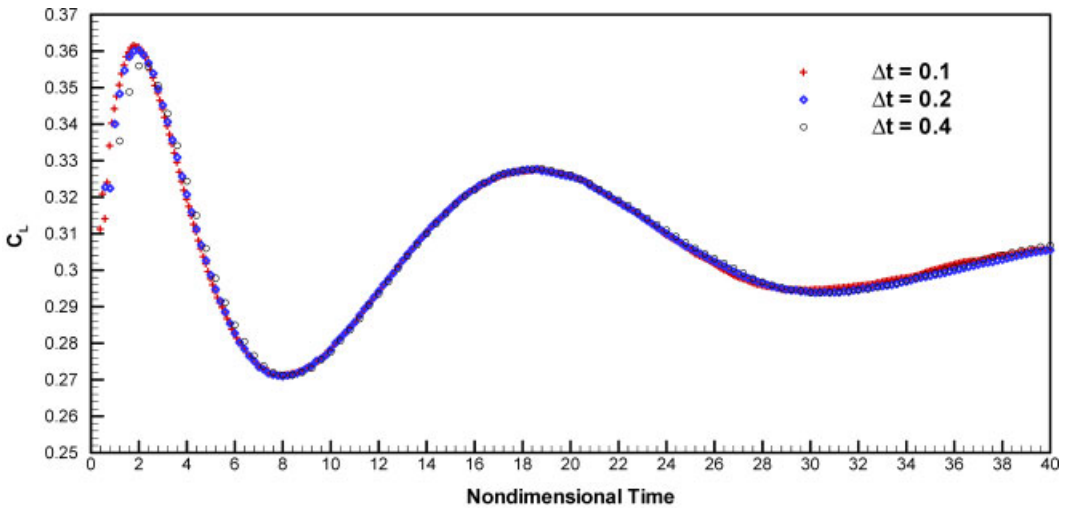

Figure 14. Dependency of time history of lift on time step size Δt: $Y_n = -0.5$, $V_\infty/\sqrt{gc} = 0.3$.

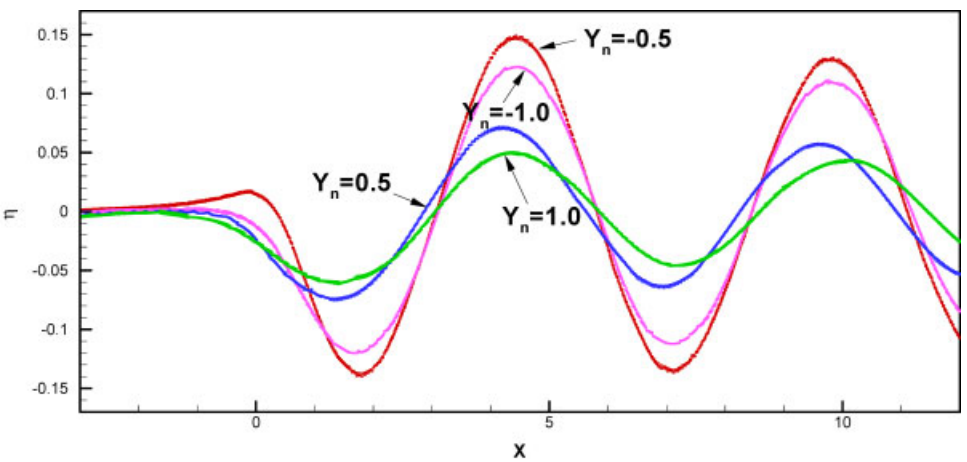

Figure 15. Variations of steady-state wave profiles according to locations of a NACA0012 section: $Y_n = -0.5, -1.0, 0.5, 1.0$; $V_\infty/\sqrt{gc} = 0.3$.

layer should be negligible for the lower layer. This is the condition which is usually used for surface wave computations: the pressure is a constant along the free surface. However, for the cases where the flow fields of upper layers are interested, for an example a surface effect wing above the free surface, it may not be practical to solve the flow field of the upper layer with a simplified condition on the pressure along the boundary.

The non-dimensionalized pressure contours near the trailing edge are magnified in Figure 11. In the figure, the grids are shown together. It can be seen that the discontinuity in the dynamic pressure along the interface is captured in one element without any oscillation or smearing.

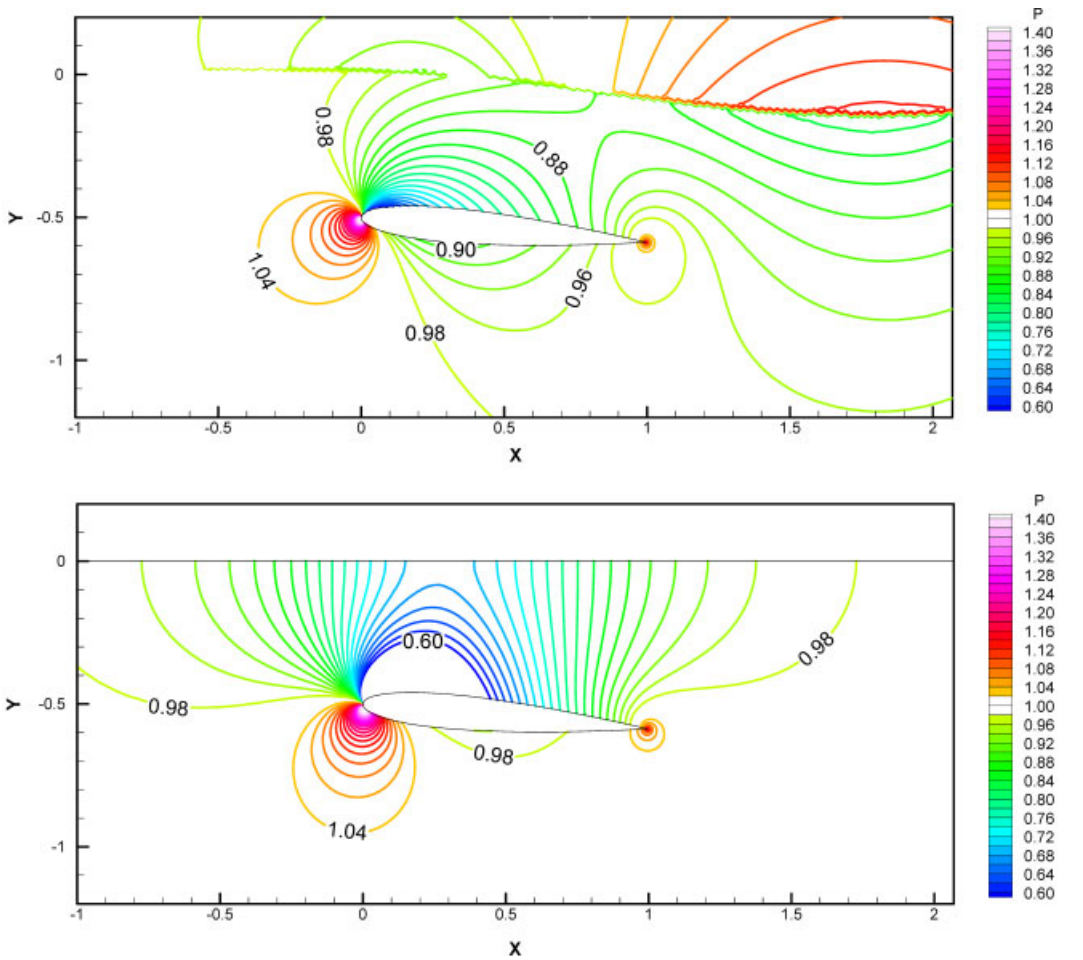

Figure 16. Comparisons of non-dimensionalized pressure contours around a NACA0012 section near an interface and a solid wall: $Y_n = -0.5$, $V_\infty/\sqrt{gc} = 0.3$.

The grid of the left side of the Figure 11 is used as a medium grid for the grid dependency study.

Grid dependency tests are carried out using three different grids which contain 4.8E4, 8.3E4 and 17.4E4 nodes, respectively. The leading edge of the wing section is located at $Y = -0.5$. In Figure 12, pressure coefficient distributions on the wing section and time histories of drag and lift coefficients are compared for the three grids. Except the results of the coarse grid, there is no significant difference for the results of the medium and fine grids. In Figure 13, the grid dependencies of the elevation of the interfaces are shown. For the rest of results, the fine grid is used. The effects of the time step size on the results are shown in Figure 14. The time step size Δt is given as 0.1, 0.2 and 0.4. Even for the case of $\Delta t = 0.4$, there is no significant difference in the calculated lift except the early stage.

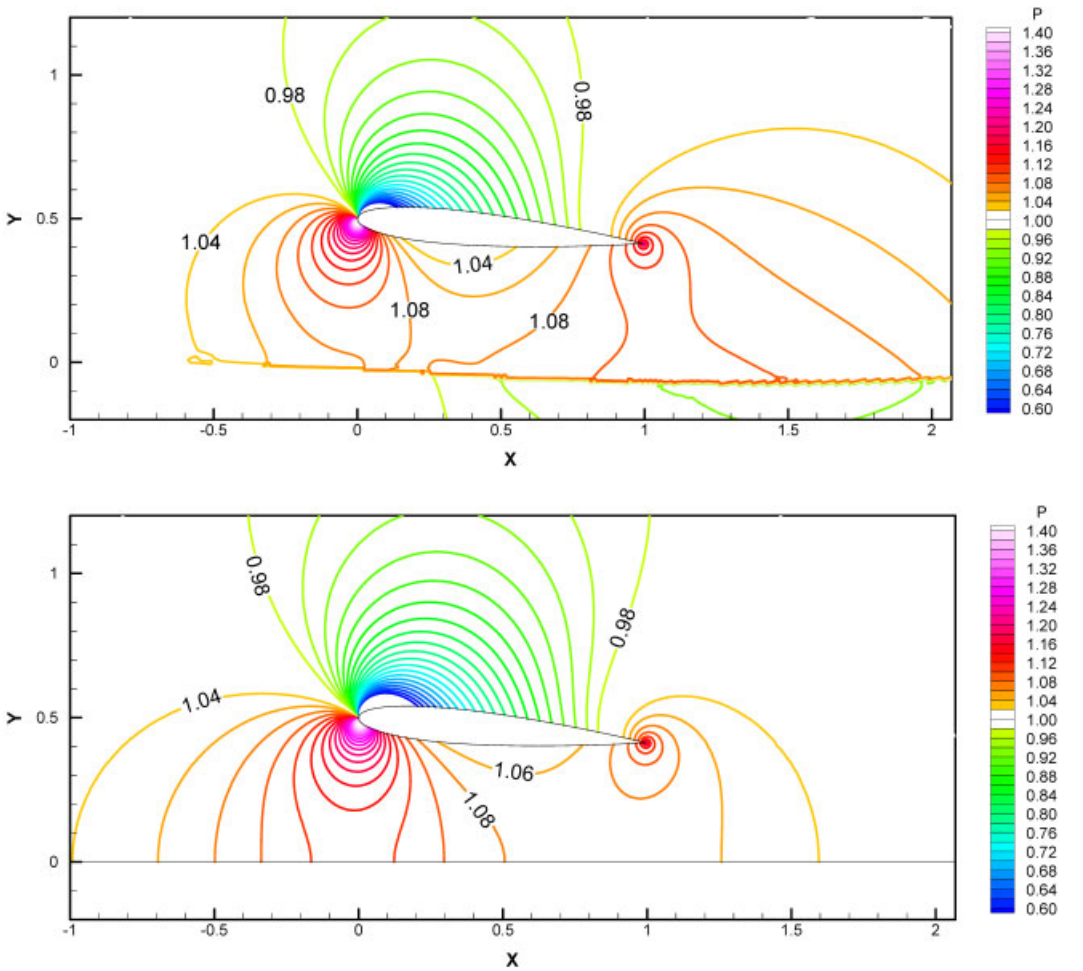

Figure 17. Comparisons of non-dimensionalized pressure contours around a NACA0012 section near an interface and a solid wall: $Y_n = 0.5$, $V_\infty/\sqrt{gc} = 0.3$.

To investigate the effects of the distance between the interface and the wing, the locations of the wing are changed for $Y_n/c = -1.0, -0.5, 0.5$ and 1.0. The calculated interface profiles of steady state are shown in Figure 15 according to the locations of the wing. Compared with the effects of the distance between the interface and the wing, it has more significant effects on the wave amplitude whether the wing is located under the interface or above the interface. However the effects of the interfaces on the lift acting on the body do not increase in proportion to the wave amplitude as shown later.

The effects of the interface on the lift acting on the body are compared with the effects of a solid wall. In Figure 16, the wing is located in the lower layer and the distance between the wing and the undisturbed interface or the solid wall is 0.5 chord. For the case of the solid wall, the acceleration near the wall starts from far upstream and there are strong pressure

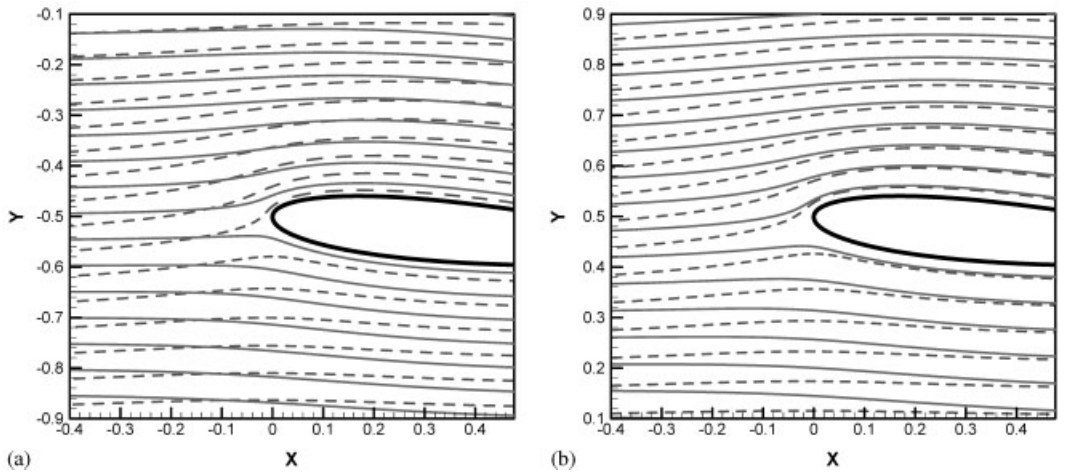

Figure 18. Comparisons of streamlines near a leading edge; solid lines: interfaces, dashed lines: solid walls: (a) $Y_n = -0.5$; and (b) $Y_n = 0.5$.

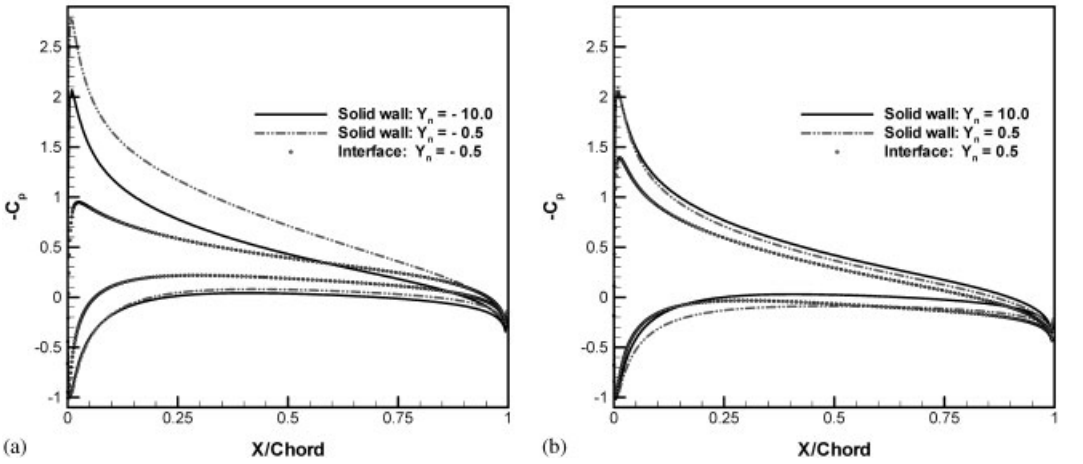

Figure 19. Variations of pressure coefficient distribution on a NACA0012 section according to distances between a leading edge and an interface/a solid wall: (a) wing under an interface/a solid wall; and (b) wing above an interface/a solid wall.

gradients along the solid wall. However for the interface case, the upstream influences are restricted to a neighbourhood of the leading edge. The pressure contours near the leading edge suggest that there is a difference in the local inflow angle between the two cases. The difference can be seen clearly in Figure 18 which shows streamlines near the leading edge for both cases. In the Figure 17, the effects of the interface and the solid wall are compared for the cases where the wing is located in the upper layer. Compared with the previous cases, the differences in the effects of the interface and the solid wall are significantly reduced.

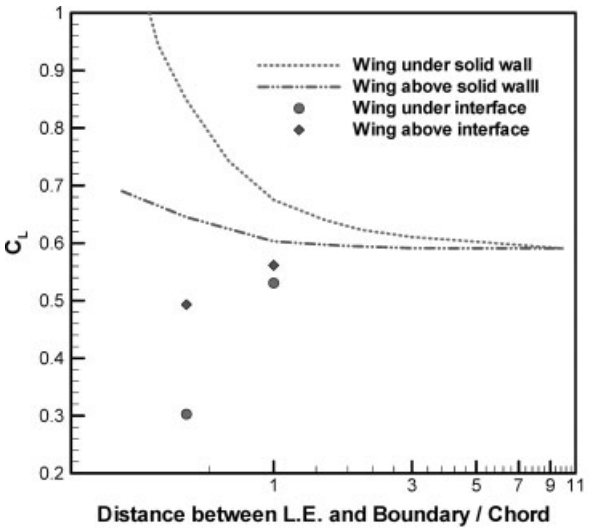

Figure 20. Variations of lift coefficient according to distances between a leading edge and an interface/a solid wall.

In Figure 18, streamlines near the leading edge are shown for the four cases. Solid lines are the streamlines of the interface cases and dashed lines are streamlines of the solid wall cases. For the interface cases, the local inflow near the leading edge seems to be more aligned with the wing and the flow turning around the leading edge is decreased. This tendency can be confirmed in Figure 19 which shows pressure coefficient distributions on the wing. For the cases of the interfaces, contributions to the lift are decreased near the leading edge especially for the case where the wing is located in the lower layer. Compared with unbounded flow fields which may be considered as flow fields of $Y_n = \pm 10$ chord, the effects of the interface appear for both suction and pressure sides. However the effects of the solid walls are dominated by pressure changes on one side which is close to the wall.

The variations of the lift acting on the wing are shown in Figure 20 according to the distances between the wing and the interfaces or solid walls. Two lines show the increases of the lift as the wing gets closer to the wall. However, for the interface cases, the lift decreases as the wing gets closer to the interface. This tendency is stronger when the wing is located in the lower layer. For the cases where the wing is under the interface or solid wall, the suction side is close to the boundary so that the effects of the boundary can be increased. Additionally, the wave elevation is larger when the wing is located in the lower layer so that the effects of the interface are increased.

4. CONCLUSIONS

The ghost fluid method has been successfully adopted to analyse the two-layer incompressible flow using an unstructured grid and an implicit method. Due to the data reconstruction at control surfaces based on the gradients, the ghost fluid method can be adopted without any

additional storage for the ghost nodes at the cost of the modification of the gradient calculations. It has been shown that the discontinuity in the non-dimensionalized pressure is captured in one element without any oscillations or smearing.

Good agreements have been achieved for the comparisons of the interface configurations with the experiments and other numerical results on the transcritical internal waves. The developed code has been applied to analyse the internal waves generated by a NACA0012 section moving near the interface. It is shown that the results are independent of the grid for the medium and fine grids. The effects of the time step size are negligible except for the largest time step size $\Delta t = 0.4$. It has been shown that the interface can reduce the lift acting on the wing significantly even though the interface elevation may not be significant. Although the lift acting on the wing increases as the wing gets closer to the solid wall, the lift decreases when the wing gets closer to the interface. The increase or decrease in the lift is more significant when the wing is located in the lower layer.

REFERENCES

1. Iafrati A, Mascio A, Campana EF. A level set technique applied to unsteady free surface flows. *International Journal for Numerical Methods in Fluids* 2001; **35**:281–297.
2. Pan D, Chang CH. The capturing of free surfaces in incompressible multi-fluid flows. *International Journal for Numerical Methods in Fluids* 2000; **33**:203–222.
3. Sussman M, Almgren AS, Bell JB, Colella P, Howell LH, Welcome ML. An adaptive level set approach for incompressible two-phase flows. *Journal of Computational Physics* 1999; **148**:81–124.
4. Sussman M, Fatemi E, Smereka P, Osher S. An improved level set method for incompressible two-phase flows. *Computers and Fluids* 1998; **27**:663–680.
5. Helenbrook BT, Martinelli L, Law CK. A numerical method for solving incompressible flow problems with a surface of discontinuity. *Journal of Computational Physics* 1999; **148**:366–396.
6. Nguyen DQ, Fedkiw RP, Kang M. A boundary condition capturing method for incompressible flame discontinuities. *Journal of Computational Physics* 2001; **172**:71–98.
7. Fedkiw RP, Aslam T, Merriman B, Osher S. A non-oscillatory Eulerian approach to interfaces in multimaterial flows (the ghost fluid method). *Journal of Computational Physics* 1999; **152**:457–492.
8. Liu TG, Khoo BC, Yeo KS. Ghost fluid method for strong shock impacting on material interface. *Journal of Computational Physics* 2003; **190**:651–681.
9. Caiden R, Fedkiw RP, Anderson C. A numerical method for two-phase flow consisting of separate compressible and incompressible regions. *Journal of Computational Physics* 2001; **166**:1–27.
10. Kang M, Fedkiw RP, Liu XD. A boundary condition capturing method for multiphase incompressible flow. *SIAM Journal on Scientific Computing* 2000; **15**:323–360.
11. Fedkiw RP. Coupling an Eulerian fluid calculation to a Lagrangian solid calculation with the ghost fluid method. *Journal of Computational Physics* 2002; **175**:200–224.
12. Shin S, Kim CK, Bai KJ. Numerical simulation on an interaction of a vortex street with an elliptical leading edge using an unstructured grid. *International Journal for Numerical Methods in Fluids* 2004; **44**:331–346.
13. Shin S, Ragab SA. Numerical simulation of streaklines of traveling vortices using a transport equation on an unstructured grid. *Computers and Fluids*, submitted.
14. Melville WK, Helfrich KR. Transcritical two-layer flow over topography. *Journal of Fluid Mechanics* 1987; **178**:31–52.
15. Grue J, Friis HA, Palm E, Rusas PO. A method for computing unsteady fully nonlinear interfacial waves. *Journal of Fluid Mechanics* 1997; **351**:223–252.

